Applied Catalysis B: Environmental 237 (2018) 295–301

Contents lists available at ScienceDirect

Applied Catalysis B: Environmental

journal homepage: www.elsevier.com/locate/apcatb

Vanadium disulfide decorated graphitic carbon nitride for super-efficient solar-driven hydrogen evolution

Mengmeng Shao[a], Yangfan Shao[a,b], Shengjie Ding[a], Jingwei Wang[c], Jinchen Xu[a], Yuanju Qu[a,d], Xiongwei Zhong[a,e], Xinman Chen[f], Weng Fai Ip[g], Ning Wang[c], Baomin Xu[e], Xingqiang Shi[b], Xuesen Wang[h], Hui Pan[a,*]

[a] Institute of Applied Physics and Materials Engineering, University of Macau, Macao SAR, PR China
[b] Department of Physics, Southern University of Science and Technology, Shenzhen, PR China
[c] Department of Physics and Institute of Nano Science and Technology, The Hong Kong University of Science and Technology, Hong Kong SAR, PR China
[d] College of Physics and Communication Electronics, Jiangxi Normal University, Nanchang, PR China
[e] Department of Materials Science and Engineering, Southern University of Science and Technology, Shenzhen, PR China
[f] Institute of Opto-electronic Materials and Technology, South China Normal University, Guangzhou, PR China
[g] Chemistry Supporting Group, Faculty of Science and Technology, University of Macau, Macao SAR, PR China
[h] Department of Physics, National University of Singapore, Singapore

ARTICLE INFO

Keywords:
g-C_3N_4
VS_2
Photocatalytic hydrogen evolution
Charge transfer
Electron-hole separation

ABSTRACT

Highly efficient, earth-abundant, and low-cost photocatalysts are widely pursued for solar-driven hydrogen generation from water. Herein, we first report vanadium disulfide (VS_2) with high hydrogen evolution reaction (HER) activity both in basal and edges to be the co-catalyst of graphitic carbon nitride (g-C_3N_4) for ultrahigh solar-driven hydrogen production. VS_2-decorated g-C_3N_4 shows an impressing photocatalytic hydrogen evolution with a rate of 87.4 μmol/h, 26 times higher than pristine g-C_3N_4. Our combined experimental and computational studies reveal that the excellent efficiency of the composite is attributed to: (1) effective electron-hole separation and electron transfer from g-C_3N_4 to VS_2, resulting from the optimal band alignment between VS_2 and g-C_3N_4 and metallic characteristic of VS_2; (2) fast hydrogen generation on the surface due to the high surface area and excellent HER activity of VS_2. Our findings demonstrate that VS_2/g-C_3N_4 may be applicable in solar-driven water splitting, and the design principle can be applied to search for novel photocatalysts.

1. Introduction

Solar-driven hydrogen production from water has been considered as a promising strategy for alleviating global energy crisis because hydrogen, as a high-density energy carrier, is clean, abundant, and renewable [1–4]. Since Honda and Fujishima first reported the water-splitting on TiO_2, the compound semiconductors, including oxides, sulfides and nitrides, have been widely investigated in photocatalytic hydrogen generation [5–12]. Although tremendous progress has been achieved, these photocatalysts still suffer from low efficiency on utilizing solar energy and poor stability [13–17]. Recently, the metal-free polymer semiconducting graphitic carbon nitride (g-C_3N_4) was found to be a promising photocatalyst for water splitting under visible light due to its satisfactory stability, and suitable band structure with a band gap of 2.7 eV [18–22]. However, the intrinsically inefficient photo-induced carriers' separation and low mobility in the g-C_3N_4 impeded its further application in photocatalysis [23,24]. It has been demonstrated that loading co-catalyst on g-C_3N_4 could largely overcome the shortcomings by attracting electrons onto co-catalyst and leaving holes behind [25–30]. Especially, the noble metals, such as Pt, are considered as the most powerful co-catalysts because they are active in hydrogen evolution reaction (HER). However, the practical application of Pt-loaded g-C_3N_4 in water-splitting is hindered by its high cost owing to its scarcity [31,32]. Therefore, extensive efforts have been carried out to search cheap, efficient, and abundant co-catalysts, such as graphene, MoS_2 and Ni_2P [33–35]. Although many active and earth abundant co-catalyst have been investigated to improve the photocatalytic performance of g-C_3N_4 in the past decade, practical application is still far away and further studies are needed.

As one of general rules on the searching of co-catalyst, the materials should show high activity of HER. Experimental and theoretical studies showed that two-dimensional (2D) transition metal dichalcogenides (TMDs) with a sandwich structure, in which the transition metal layer is between two layers of the chalcogen elements, were catalytically active

* Corresponding author.
E-mail address: huipan@umac.mo (H. Pan).

https://doi.org/10.1016/j.apcatb.2018.05.084
Received 20 April 2018; Received in revised form 24 May 2018; Accepted 28 May 2018
Available online 29 May 2018

in HER [36–40]. For example, MoS_2, WS_2, $MoSe_2$, and WSe_2 showed active HER performance at their metallic edges [40–42]. MoS_2 had been used as co-catalyst to enhance photocatalytic activity of g-C_3N_4 [43]. However, these TMDs were inert on their basal planes, which limited their roles in photocatalytic performance [44,45]. Therefore, the TMDs with high catalytic HER activity both at edge and on basal plane are desirable for effective co-catalysts in water-splitting. Recently, theoretical calculations predicted that both edge and basal sites of VS_2 were quite active in HER [46–49], and the experimental results further confirmed that the VS_2 exhibited better HER performance than MoS_2 and WS_2 [50–52]. Therefore, it is worthwhile to explore if VS_2 can be an effective co-catalyst for benefiting hydrogen production in photocatalytic reaction, which has not been reported so far.

In this work, we design and fabricate VS_2-decorated g-C_3N_4 (VS_2/g-C_3N_4) as an efficient photocatalyst for water splitting. The VS_2/g-C_3N_4 shows a super-high photocatalytic performance with a hydrogen production of 87.4 μmol/h. The excellent photocatalytic activity of VS_2/g-C_3N_4 is mainly attributed to VS_2 that serves as photo-induced electron trapping and transportation media, leading to the fast separation of electron-hole pairs and efficient transportation of electrons, and that has thermal-neutral Gibbs free energy for hydrogen adsorption, enhancing photocatalytic redox reactions accordingly.

2. Experimental section

2.1. Chemicals and regents

Melamine ($C_3N_3(NH_2)_3$, Macklin, 99%), sodium orthovanadate ($Na_3VO_4{\cdot}12H_2O$ Aladdin, 99%), thioacetamide (CH_3CSNH_2, Aladdin, 98%), Triethanolamine (TEOA, Aladdin, 98%), ethanol (CH_3CH_2OH, Aladdin, 99%), sodium sulfate (Na_2SO_4, Aladdin, 99%), sodium sulfite (Na_2SO_3, Aladdin, 98%), sodium sulfide nonahydrate ($Na_2S{\cdot}9H_2O$, Aladdin, 98%), were used without further purification. Water used in our experiments was deionized.

2.2. Preparation of VS_2/g-C_3N_4

Firstly, the g-C_3N_4 was synthesized by heating the precursor-melamine (10 g) in a covered alumina crucible at 550 °C for 4 h with a heating rate of 5 °C/min. Then, the yellow powder was ground [53]. Then the VS_2 decorated g-C_3N_4 was prepared by one-pot hydrothermal process. Typically, 1 g of g-C_3N_4 was dispersed in 10 mL ethanol aqueous by sonicating for 30 min. 96 mg sodium orthovanadate ($Na_3VO_4{\cdot}12H_2O$) and 90 mg thioacetamide (CH_3CSNH_2) were added into 30 mL deionized (DI) water and stirred for 30 min (n_v:n_s = 1:5). Then, the above solution (containing V and S sources) was added into the g-C_3N_4 suspension stirred for 30 min. Finally, the mixed solution was transferred to 50 mL Teflon-lined stainless steel autoclave and kept at 160 °C for 24 h. The resulting materials were filtrated, washed with DI water and dried in vacuum to obtain the solid sample labeled as VSCN-2.8, where the weight ratio of VS_2 to g-C_3N_4 was 2.8 wt% and the weight of VS_2 was calculated from V source. The residual specimen VS_2/g-C_3N_4 with different VS_2 weight contents of about 0.1 wt%, 0.7 wt %, 1.4 wt% and 5.6 wt% were prepared with the same method by adding different mass of $Na_3VO_4{\cdot}12H_2O$ and CH_3CSNH_2, and labeled as VSCN-0.1, VSCN-0.7, VSCN-1.4 and VSCN-5.6, respectively. Pure VS_2 (by the same process without adding g-C_3N_4) and hydrothermal-treated g-C_3N_4 (treated by hydrothermal process without adding V and S sources) were also prepared for comparison.

2.3. Materials characterization

X-ray diffractometer (XRD, Rigaku Smartlab) with Cu Kα radiation (λ = 0.154 nm) was used to record the crystalline phase of samples. Transmission electron microscopy (TEM) images and energy dispersive spectrometer (EDS) element mapping were acquired by using Talos F200S. Scanning electron microscopy (SEM, Zeiss Sigma) was used to capture the morphology of sample. Chemical valence of sample was investigated by X-ray photoelectron spectroscopy (XPS) with monochromatic Al Kα X-ray (Thermo Fisher Scientific). N_2 adsorption-desorption isotherm was performed by using Micromeritics 3Flex instrument to analyze the Brunauer-Emmett-Teller (BET) surface area and pore volume of catalysts. UV–vis diffuse reflectance spectrum (UV–vis DRS) was carried out by Shimadzu UV-2600 spectrometer equipped with integrating sphere, and $BaSO_4$ as reference. Photoluminescence (PL) spectrum was collected under 325 nm excitation light by Shimadzu RF-5301 fluorescence spectrometer.

Photoelectrochemical performance was tested using electrochemical workstation (Modulab 8 slot chassis, Solartron) with a standard three-electrode cell in which the working electrodes of g-C_3N_4 and VSCN-2.8 were deposited on carbon paper. 0.1 M $NaSO_4$ + 0.1 M Na_2SO_3 + 0.01 M Na_2S mixed aqueous solution was used as the electrolyte, Pt foil as the counter electrode and Ag/AgCl (saturated KCl) as the reference electrode. An AM 1.5 solar simulator (100 mW/cm^2, Abet Technologies) was applied as the light source. Electrochemical impedance spectroscopy (EIS) was measured under the open-circle potential and light irradiation with frequency ranging from 0.01 to 100 kHz and amplitude of 0.01 V. The photocurrent was carried out under intermittent illumination with the potential of 0.4 V vs Ag/AgCl.

2.4. Photocatalytic hydrogen generation

The photocatalytic hydrogen generation of the as-prepared VSCN was evaluated by adding 50 mg of photocatalyst into 85 mL TEOA aqueous solution (10 vol%) in side-irradiation quartz vessel at room temperature. The reaction system was sonicated for 15 min to disperse photocatalyst uniformly and then bubbled with N_2 to remove the air prior to light irradiation. At regular intervals, the gas product (about 0.4 mL) was quantified by Agilent gas chromatography (GC7890B) with N_2 as the carrier gas and TCD (Thermal Conductivity Detector) as the detector. For the stability test of photocatalytic H_2-production over the prepared samples, the reaction system (50 mg photocatalyst and 85 mL TEOA solution) was bubbled with N_2 to remove the air before every recycling. Then, recycling reaction was carried out under stirring for 7 cycles.

The apparent quantum yield (AQE) of the photocatalyst was measured under AM 1.5 solar simulator with 420 nm monochromatic light filter. The average power intensity of 420 nm monochromatic light was about 14.3 mW/cm^2. The AQE is calculated as follows:

$$\mathrm{AQE}(\%) = \frac{\text{Number of produced } H_2 \times 2}{\text{Number of incident photons}}$$

3. Results and discussion

3.1. Structures and characterizations

The XRD patterns of the g-C_3N_4 and VS_2/g-C_3N_4 show two obvious Bragg peaks (Fig. 1a). The broad peak at around 27.5° is indexed to the (002) lattice plane that is related to the stacking of aromatic segments. Another peak at around 13.0°, indexed to the (100), results from the in-plane repeat of tri-s-triazine units, indicating an interplanar separation of ~0.68 nm [54]. Meanwhile, a new sharp peak appears at around 10.7° in all VS_2/g-C_3N_4 (VSCN) samples, corresponding to an interplanar separation of 0.83 nm. The interplanar separation increases from 0.68 to 0.83 nm due to the partial oxidation and hydrolysis of the tertiary amino group in g-C_3N_4, and the introduction of secondary amino groups (−NH) and hydroxyl groups (−OH) [55]. Our computational result also shows the oxidation and hydrolysis result in the expansion (Fig. S1b). Compared to the g-C_3N_4, the (100) diffraction peak of VS_2/g-C_3N_4 shifts slightly towards smaller angle because of the local disorder in the structure by introducing −NH and −OH groups. The other two

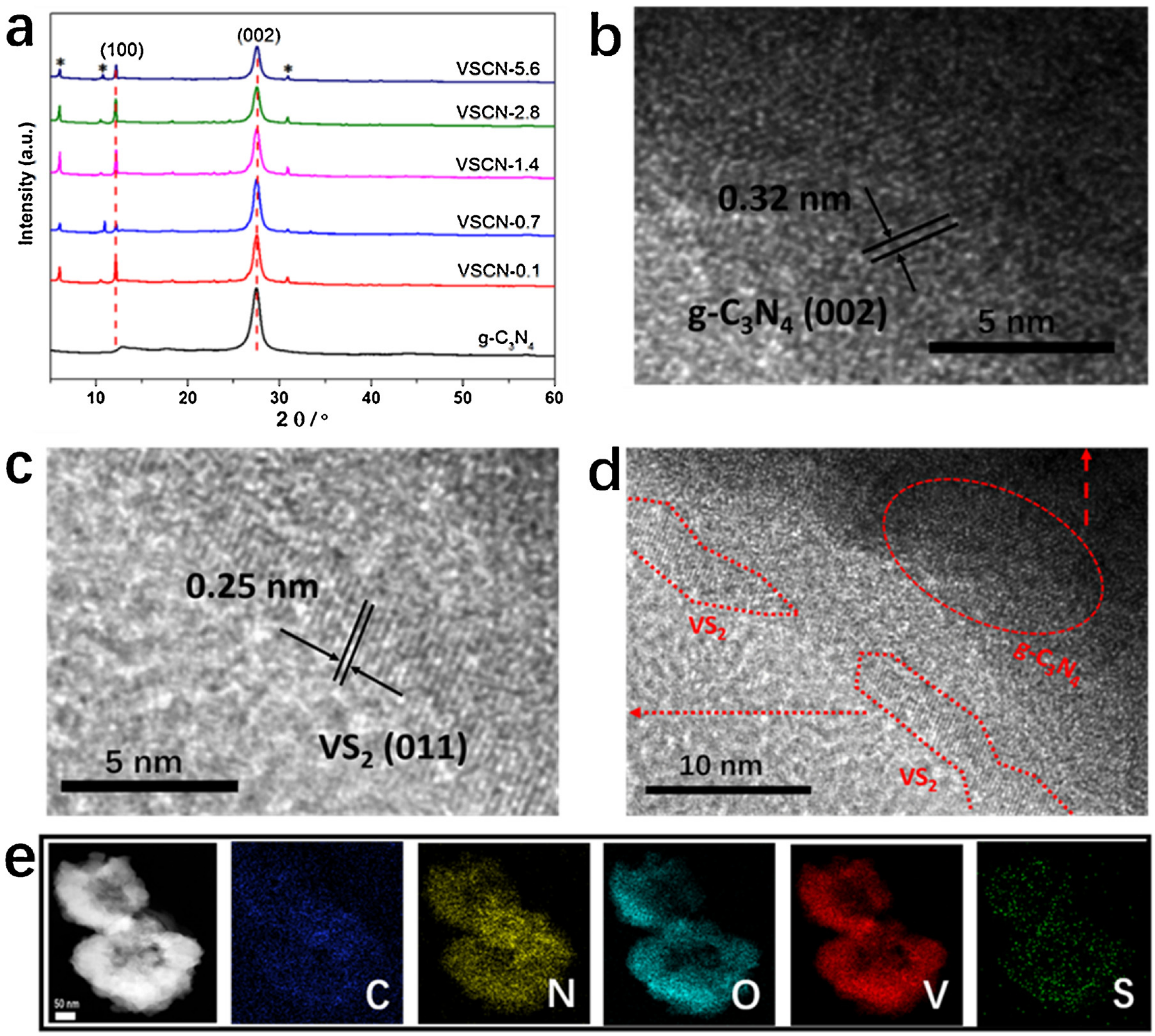

Fig. 1. The structure and morphology. (a) XRD patterns of g-C_3N_4 and VS_2/g-C_3N_4. (b) and (c) HRTEM images of g-C_3N_4 and VS_2 in TEM image (d). (e) EDS elemental mappings for VS_2/g-C_3N_4.

new peaks with narrow width at 6.04° and 30.9° show the improved crystallinity of the VS_2/g-C_3N_4 after hydrothermal process (Fig. 1a and S1a) [55,56]. Although there are no obvious diffraction peaks of VS_2 in the composites due to its low content, the TEM and HRTEM images of VS_2/g-C_3N_4 (Fig. 1b-d) demonstrate clearly the existences of VS_2 and g-C_3N_4. Moreover, the EDS elemental mapping (Fig. 1e) also confirms the existence of C, N, O, V, and S elements. The SEM images (Fig. S1c-d and S2) further show the morphology of VS_2/g-C_3N_4 becomes loose and many pores appear on the surface, leading to the increase of surface area.

The composition of VS_2/g-C_3N_4 and chemical bonding state of each element were further investigated by XPS (Fig. 2). The binding energies at 288.5 and 284.8 eV in the C 1 s XPS spectrum (Fig. 2a) are related to the N−C = N and C−C, respectively [54,57]. A weak shoulder peak at 289.7 eV results from the C–O (or O=C–O) formed in the hydrothermal process, indicating the partial hydrolysis of g-C_3N_4 [58], consistent with the XRD results (Fig. 1a). Three obvious peaks at 399.1 eV, 400.4 eV and 401.5 eV in the N 1s (Fig. 1b) are corresponding to C–N=C, N−(C)$_3$ and N−H, respectively. The V 2p signals at 516.2 eV and 523.4 eV (Fig. 2c) are contributed to V $2p_{3/2}$ and V $2p_{1/2}$, implying the existence of V^{4+}. Other V 2p peaks at 517.5 eV ($2p_{3/2}$) and 524.8 eV ($2p_{1/2}$) belong to V^{5+} (V_2O_5) [51,59]. The XPS spectrum of O 1s shows two signals, which are related to V−O (530.8 eV) and N-C–O (532.2 eV) groups [59,60], suggesting that V is inevitably partially oxidized to V_2O_5 in the hydrothermal process. The S 2p peaks at 162.8 eV and 163.7 eV are ascribed to the S^{2-} species, indicating the formation of VS_2.[45] Other peaks at 167.5 eV and 168.9 eV arise from sulfite (SO_3^{2-}) [61]. Compared to the pure g-C_3N_4 and VS_2 (Fig. S3), the N 1s in the VS_2/g-C_3N_4 shifts to high binding energy, while the V 2p (V^{4+}) in the VS_2/g-C_3N_4 shifts to low binding energy, indicating the strong interaction between VS_2 and g-C_3N_4 [62,63]. Our XPS results further confirm that VS_2/g-C_3N_4 composite is obtained and both VS_2 and g-C_3N_4 undergo partial oxidation in the hydrothermal process.

3.2. Photocatalytic performance of hydrogen evolution

Our characterizations clearly demonstrate that VS_2-decorated g-C_3N_4 is successfully fabricated by the hydrothermal reaction. The well-known HER activity of VS_2 should promote the photocatalytic performance of g-C_3N_4. To confirm our design, we carried out the photocatalytic H_2 evolution tests on the as-synthesized composites (Fig. 3). The pure g-C_3N_4 displays inferior photocatalytic performance (Fig. 3a), and its activity is enhanced by 2.7 times after hydrothermal treatment (Fig. S5) because of the introduction of oxygen group [55], and the improvement of electron-hole separation. Our experiments confirm that VS_2 as co-catalyst for hydrogen evolution can dramatically improve the photocatalytic activity of g-C_3N_4 (Fig. 3a). We also find that the weight ratio of VS_2 plays an important role on the improvement of performance of g-C_3N_4. With 0.1 wt% VS_2 in the composite, the hydrogen evolution rate of the g-C_3N_4 is increased by nearly 3-fold. Surprisingly,

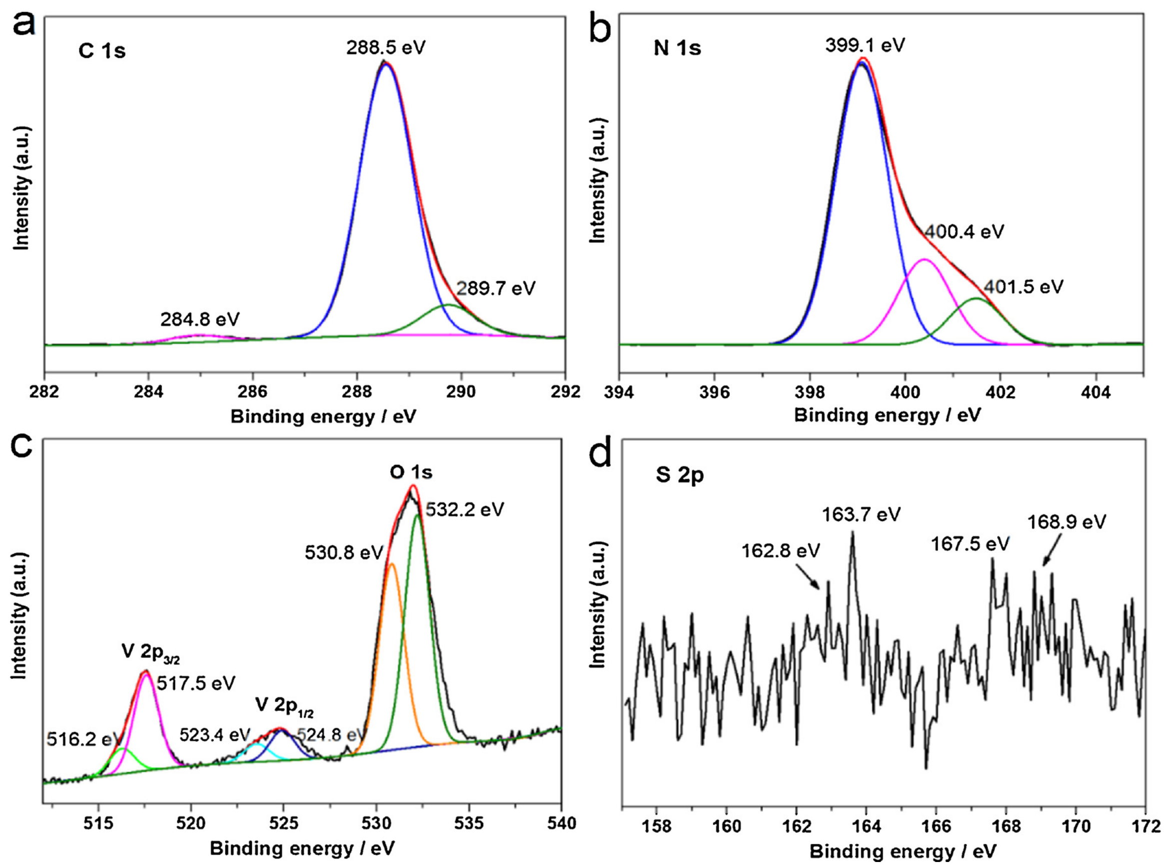

Fig. 2. XPS spectrum of VS_2/g-C_3N_4. (a) C 1s. (b) N 1s. (c) V 2p and O 1s. (d) S 2p.

the photocatalytic performance of g-C_3N_4 is enhanced further with increasing the VS_2 loading up to 2.8 wt%. Especially, the g-C_3N_4 with a VS_2 loading of 2.8 wt% shows a super high photocatalytic H_2-production rate of 87.4 μmol/h, which is much higher than those of pristine g-C_3N_4 (3.3 μmol/h), g-C_3N_4 after hydrothermal treatment (8.9 μmol/h) and physically mixed g-C_3N_4 and VS_2 (7.2 μmol/h) (Fig. S5). The apparent quantum efficiency (AQE) of g-C_3N_4 with 2.8% VS_2 (VSCN-2.8) at 420 nm is 5.5%. Therefore, VS_2 plays an important role in improving the photocatalytic H_2-evolution of VSCN. Furthermore, comparing to g-C_3N_4 with other co-catalysts (Fig. 3a and Table S1), the VSCN-2.8 still exhibits competitive/higher photocatalytic performance. Further increasing the amount of VS_2, however, results in the reduction of photocatalytic activity. Because the excessive VS_2 loading may cover the surface of g-C_3N_4, reduce the surface area and hinder the utilization of light. As V_2O_5 was observed on the surface of the sample by XPS (Fig. 2c), the photocatalytic performance of V_2O_5/g-C_3N_4 was tested. We find the photocatalytic hydrogen evolution of V_2O_5/g-C_3N_4 is almost same as to that of pure g-C_3N_4 (Fig. S5), indicating that the effect of V_2O_5 can be excluded in the photocatalytic improvement of g-C_3N_4.

For practical application, the stability of photocatalyst was investigated by performing the photocatalytic reaction for 7 cycles. Our measurement shows that there is no significant decrease in the photocatalytic activity of VSCN-2.8 after 7 cycles (Fig. 3b). The characterizations on the cycled VSCN-2.8 show that the crystal structure,

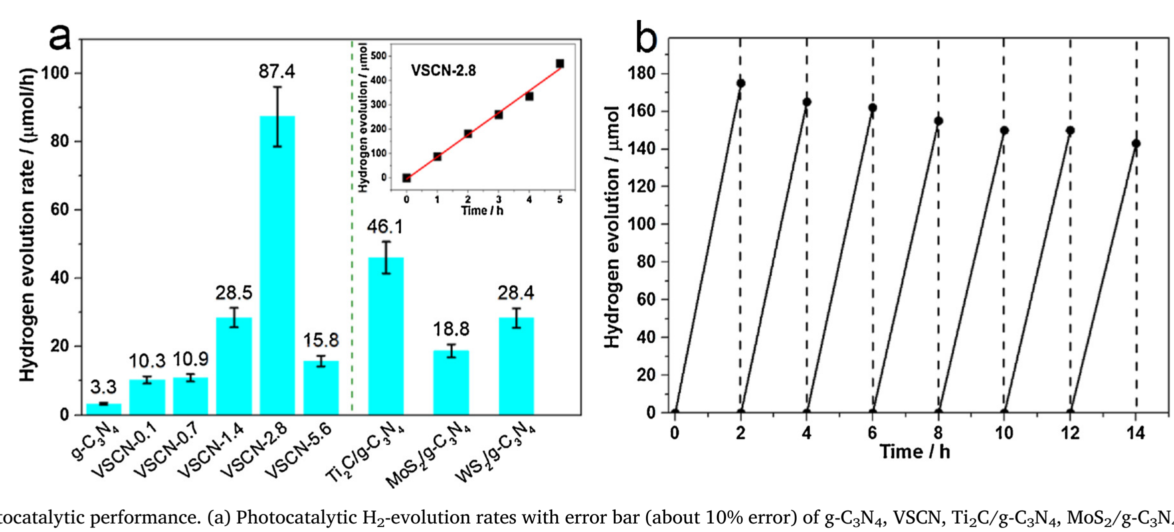

Fig. 3. Photocatalytic performance. (a) Photocatalytic H_2-evolution rates with error bar (about 10% error) of g-C_3N_4, VSCN, Ti_2C/g-C_3N_4, MoS_2/g-C_3N_4, and WS_2/g-C_3N_4. (b) Recycling test of H_2-production over VSCN-2.8. Inset of (a): Time course of H_2-evolution over VSCN-2.8.

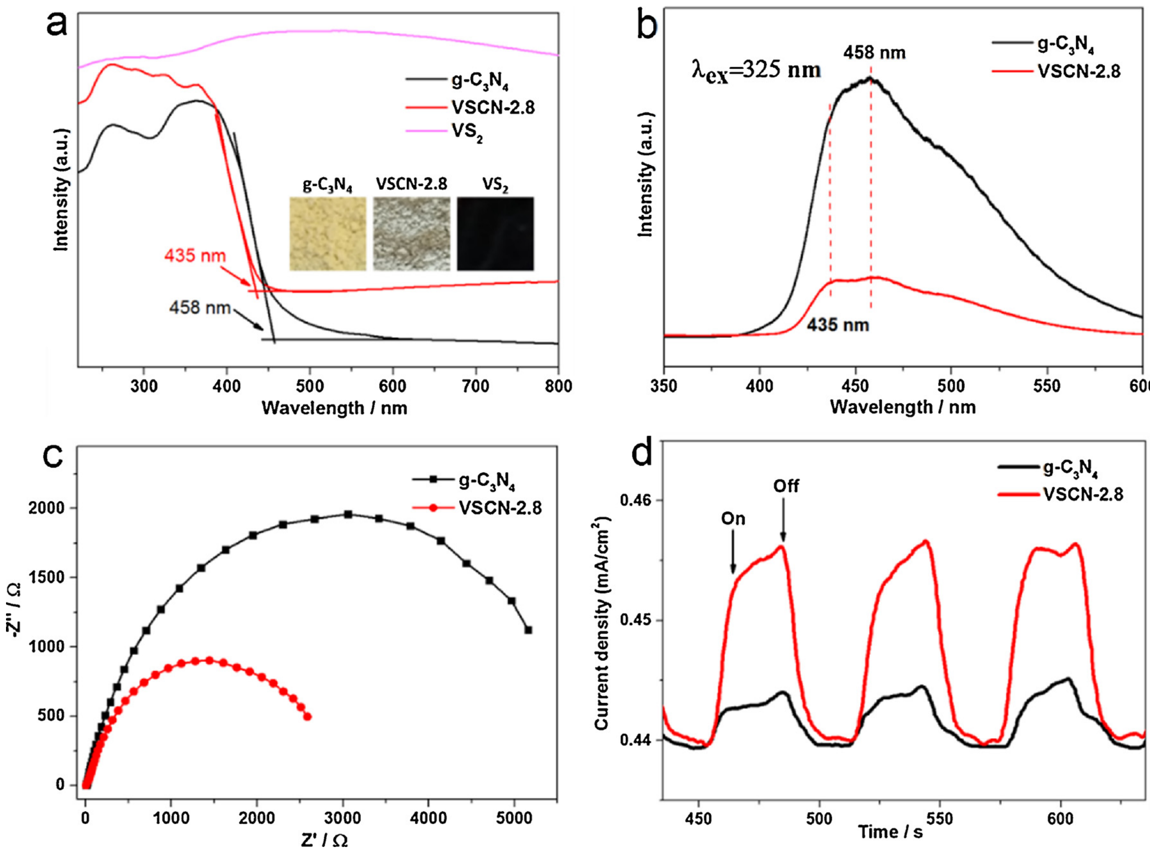

Fig. 4. Spectroscopy and photoelectrochemical characterization of g-C_3N_4 and VSCN-2.8. (a) UV–vis DRS. (b) PL spectra with 325 nm excitation. (c) EIS Nyquist plots under open circle potential and light irradiation. (d) Transient photocurrent responses at 0.4 V vs Ag/AgCl.

chemical composition, oxidation state and light absorption have changed little from those of as-prepared sample (Fig. S7), indicating that VSCN-2.8 is highly stable.

3.3. Photocatalytic mechanism

To figure out the underline origin of the improved performance of VS_2/g-C_3N_4, three main photocatalytic processes, including optical absorption, charge separation and transfer, and redox reaction on the surface, were characterized [64]. The absorption spectrum of g-C_3N_4 shows that its bandgap is 2.7 eV (458 nm, Fig. 4a), in good agreement with literature [19]. The VSCN-2.8 shows a slight blue shift on absorption spectrum (435 nm, 2.8 eV). Similar phenomenon is also observed on pure g-C_3N_4 with hydrothermal treatment (Fig. S8a). The blue shift is induced by the partial oxidation of g-C_3N_4 and introduction of electron withdrawing groups (C–O groups) during hydrothermal treatment, which result in the down shifting of both conduction and valence bands. The valence band shifts down more than the conduction band, resulting in the blue shift of absorption edge and the increase of the bandgap [65]. Therefore, the light utilization has no improvement, and the dramatically improved activity of VS_2-decorated g-C_3N_4 should be induced by other factors.

To explore the efficiency of charge separation and transfer, we performed the tests of photoluminescence (PL) and electrochemical impedance spectrum (EIS). We find that the PL intensity of VSCN-2.8 is much weaker than that of g-C_3N_4 (Fig. 4b), implying the recombination of photo-induced charges can be effectively suppressed in the VSCN-2.8 [66]. The PL intensity of the VSCN samples gradually decrease with the increase of VS_2 weight percentage (Fig. S9). The VSCN-2.8 and VSCN-5.6 show lowest PL intensity among those samples, indicating the improved photo-generated charge separation. Moreover, another PL emission peak around 435 nm appears in VSCN-2.8 besides the peak at 458 nm, which is consistent with the adsorption result (Fig. 4a). The EIS plots (Fig. 4c and Fig. S10b) reveal that the VSCN-2.8 has the smallest semicircle diameter comparing to g-C_3N_4 and other VS_2-decorated g-C_3N_4, demonstrating its lowest charge transfer resistance [66]. Importantly, a smaller arc is available for the VSCN-2.8 under light irradiation relative to that in dark (Fig. S10a), suggesting the photo-generated charge can be effectively transferred to the reaction surface under illumination. We see that the photocurrent of the VSCN-2.8 is about three times higher than that of the g-C_3N_4 (Fig. 4d) due to the efficient photo-induced charge separation and transfer.

To further investigate the mechanism of electron-hole pair separation and transfer, the electronic property of VS_2 was calculated (see Computational section in Supplementary data). Our first-principles calculations (Fig. 5a) show that VS_2 is metallic, as indicated by the high free-carrier density around the Fermi level. The Fermi level of VS_2 is about 1.03 eV (vs. SHE, Fig. S13a) and more positive than the conduction band (CB) of g-C_3N_4 (around -1.14 eV vs. SHE). Therefore, the photo-induced electrons can easily transfer from g-C_3N_4 to VS_2, and then those electrons are rapidly shuttled to the surface reactive sites for H_2 evolution reaction due to the metallicity of VS_2. Thus, the high photo-induced charge separation and transfer activity are contributed to the metallicity of VS_2 and the optimal band alignment between VS_2 and g-C_3N_4.

During the redox reaction for hydrogen generation, the surface area of photocatalyst plays an important role. The large surface area leads to abundant surface reactive sites and then boost hydrogen evolution on the surface. Therefore, the adsorption-desorption isotherms were carried out to compare the surface area of the g-C_3N_4 and VSCN composites. The surface area of g-C_3N_4 is greatly increased by VS_2-decoration and hydrothermal treatment (Table S2 and Fig. S11) due to increased pores on the surface of g-C_3N_4 after hydrothermal treatment and VS_2-decoration (Fig. S1c-d and S2). Particularly, the surface area of VS_2/g-

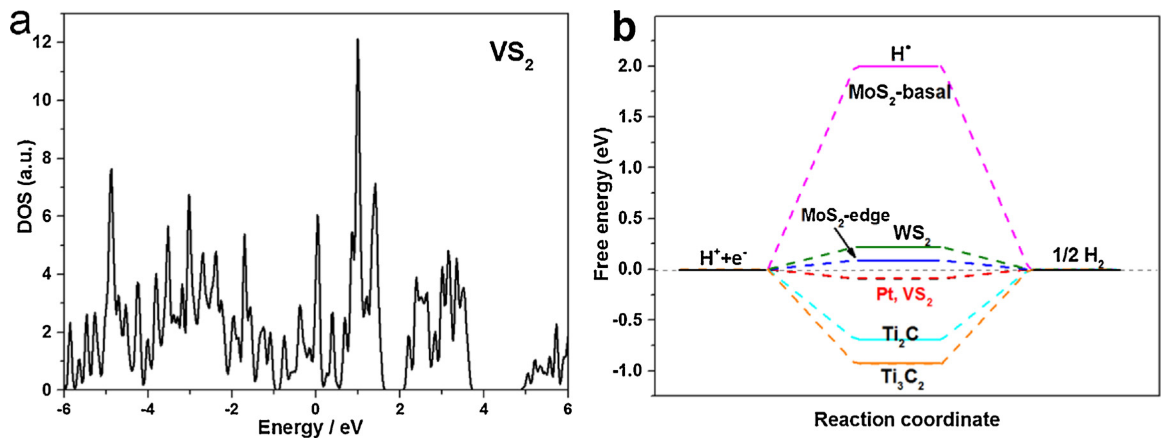

Fig. 5. Theoretical calculation results of VS_2. (a) The total density of states (DOS) for VS_2. (b) The calculated free-energy (ΔG_{H^*}) of VS_2 and the referenced Pt (ref. [68]), MoS_2-basal (ref. [70]), MoS_2-edge (ref. [67]), WS_2 (ref. [71]), Ti_3C_2 (ref. [64]) and Ti_2C.

C_3N_4 increases gradually with the loading of VS_2 up to 2.8 wt%, and then decreases with further increasing the VS_2 loading due to the agglomeration of VS_2. The VSCN-2.8 composite with the highest surface area has abundant surface reactive sites, leading to efficient hydrogen generation on the surface.

Moreover, the HER performance of VS_2 is also crucial to the surface redox reaction. We calculated the Gibbs free energy of hydrogen adsorption (ΔG_{H^*}) to explore the HER performance of VS_2, which is considered as an appropriate descriptor of HER activity. The ΔG_{H^*} of outstanding HER catalyst should be close to zero for thermal-neutral reactions [67]. Pt is regarded as the most ideal HER catalyst with the ΔG_{H^*} of -0.09 eV [68], and our calculated ΔG_{H^*} value of VS_2 is about -0.088 eV, which is comparable to the Pt catalyst (Fig. 5b and Fig. S13b). Importantly, the $|\Delta G_{H^*}|$ of VS_2 is also much smaller than those of the common transition metal sulfides (such as MoS_2 and WS_2) and MXenes (Ti_2C and Ti_3C_2). Therefore, the co-catalyst VS_2 with impressing HER activity can efficiently promote fast H_2-evolution on its surface.

Based on the theoretical calculations and experimental results, the photocatalytic mechanism of VS_2/g-C_3N_4 is proposed as follows: firstly, the electrons in the valence band (VB) of g-C_3N_4 are excited to its conduction band (CB) under the light irradiation; secondly, the intimate contact between g-C_3N_4 and VS_2 rises the Fermi level and reaches equilibrium in VS_2/g-C_3N_4 (Fig. 6 and S14) [69]; then, the photo-induced electrons transfer easily to VS_2 due to its suitable band structure and excellent metallicity, leading to efficient electron-hole separation; finally, the protons are fast reduced to H_2 by those electrons accumulated on the surface of VS_2 due to its remarkable HER activity (Fig. 6). Therefore, the optimal physical and chemical properties of VS_2/g-C_3N_4 hybrid result in ultra-high photocatalytic H_2 evolution.

4. Conclusions

In this work, we design and fabricate an efficient photocatalyst, VS_2/g-C_3N_4, for solar-driven hydrogen production, where VS_2 serves as the co-catalyst. The VS_2/g-C_3N_4 hybrid shows an ultra-high photocatalytic activity on hydrogen generation with a rate of 87.4 μmol/h, and a quantum efficiency (AQE) of 5.5%. Based on the experimental and computational results, we propose that the remarkable photocatalytic activity of VS_2/g-C_3N_4 is contributed to the effective separation of photo-generated carriers, the rapid electron transfer from g-C_3N_4 to VS_2, and the excellent hydrogen evolution on VS_2 surface. Furthermore, the VS_2/g-C_3N_4 remains high photocatalytic performance after cycles, exhibiting favorable stability and reproducibility. We expect that the VS_2/g-C_3N_4 can be noble-metal free photocatalyst for practical application in water-splitting. Our design and findings will provide guidance to explore cheap and abundant materials as catalysts for applications in photocatalysis.

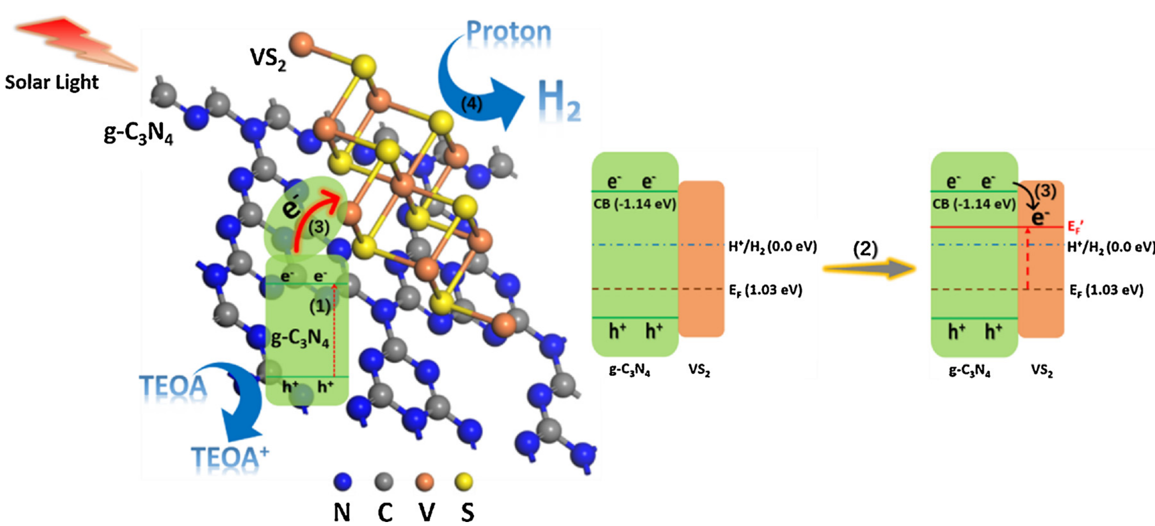

Fig. 6. The mechanism of photocatalytic hydrogen evolution on VSCN. The main photocatalytic processes are: (1) the formation of photo-induced electron and hole on g-C_3N_4; (2) the Fermi level rises and reaches equilibrium in VSCN; (3) the electrons transfer to VS_2; (4) the protons are reduced to evolve H_2 on VS_2 surface.

Acknowledgements

This work was supported by the Science and Technology Development Fund from Macau SAR (FDCT-132/2014/A3) and Multi-Year Research Grants (MYRG2017-00027-FST and MYRG2018-00003-IAPME) from Research & Development Office at University of Macau as well as a Singapore MOE AcRF grant (R-144-000-365-112). The DFT calculations were performed at High Performance Computing Cluster (HPCC) of Information and Communication Technology Office (ICTO) at University of Macau.

Appendix A. Supplementary data

Supplementary material related to this article can be found, in the online version, at doi:https://doi.org/10.1016/j.apcatb.2018.05.084.

References

[1] X. Wang, F. Wang, Y. Sang, H. Liu, Adv. Energy Mater. 7 (2017) 1700473–1700488.
[2] X. Chen, S. Shen, L. Guo, S.S. Mao, Chem. Rev. 110 (2010) 6503–6570.
[3] A. Kudo, Y. Miseki, Chem. Soc. Rev. 38 (2009) 253–278.
[4] H. Pan, Renew. Sust. Energy Rev. 57 (2016) 584–601.
[5] A. Fujishima, K. Honda, nature 238 (1972) 37–38.
[6] X. Chen, L. Liu, Y.Y. Peter, S.S. Mao, Science 331 (2011) 746–750.
[7] D. Jing, L. Guo, J. Phys. Chem. B 110 (2006) 11139–11145.
[8] K. Maeda, T. Takata, M. Hara, N. Saito, Y. Inoue, H. Kobayashi, K. Domen, J. Am. Chem. Soc. 127 (2005) 8286–8287.
[9] H. Pan, B. Gu, Z. Zhang, J. Chem. Theory Comput. 5 (2009) 3074–3078.
[10] H. Pan, X. Qiu, I.N. Ivanov, H.M. Meyer, W. Wang, W. Zhu, M.P. Paranthaman, Z. Zhang, G. Eres, B. Gu, Appl. Catal. B-Environ. 93 (2009) 90–95.
[11] M.S. Zhu, C.Y. Zhai, M. Fujitsuka, T. Majima, Appl. Catal. B-Environ. 221 (2018) 645–651.
[12] P.Y. Kuang, P.X. Zheng, Z.Q. Liu, J.L. Lei, H. Wu, N. Li, T.Y. Ma, Small 12 (2016) 6735.
[13] R. Lv, T. Wang, F. Su, P. Zhang, C. Li, J. Gong, Nano Energy 7 (2014) 143–150.
[14] D.P. Kumar, H. Park, E.H. Kim, S. Hong, M. Gopannagari, D.A. Reddy, T.K. Kim, Appl. Catal. B-Environ. 224 (2018) 230–238.
[15] H. Pan, Y.-W. Zhang, Nano Energy 1 (2012) 488–493.
[16] A.J. Rettie, K.C. Klavetter, J.-F. Lin, A. Dolocan, H. Celio, A. Ishiekwene, H.L. Bolton, K.N. Pearson, N.T. Hahn, C.B. Mullins, Chem. Mater. 26 (2014) 1670–1677.
[17] P.Y. Kuang, Y.Z. Su, G.F. Chen, Z. Luo, S.Y. Xing, N. Li, Z.Q. Liu, Appl. Surf. Sci. 358 (2015) 296–303.
[18] Z.C. Sun, M.S. Zhu, M. Fujitsuka, A.J. Wang, C. Shi, T. Majima, ACS Appl. Mater. Interfaces 9 (2017) 30583–30590.
[19] X. Wang, K. Maeda, X. Chen, K. Takanabe, K. Domen, Y. Hou, X. Fu, M. Antonietti, J. Am. Chem. Soc. 131 (2009) 1680–1681.
[20] J.C. Bian, Q. Li, C. Huang, J.F. Li, Y. Guo, M. Zaw, R.Q. Zhang, Nano Energy 15 (2015) 353–361.
[21] J.C. Bian, L.F. Xi, C. Huang, K.M. Lange, R.Q. Zhang, M. Shalom, Adv. Energy Mater. 6 (2016) 1600263.
[22] J.C. Bian, C. Huang, R.Q. Zhang, ChemSusChem 9 (2016) 2723–2735.
[23] G. Liu, P. Niu, C. Sun, S.C. Smith, Z. Chen, G.Q. Lu, H.-M. Cheng, J. Am. Chem. Soc. 132 (2010) 11642–11648.
[24] Z.-A. Lan, G. Zhang, X. Wang, Appl. Catal. B-Environ. 192 (2016) 116–125.
[25] S. Liang, Y. Xia, S. Zhu, S. Zheng, Y. He, J. Bi, M. Liu, L. Wu, Appl. Surf. Sci. 358 (2015) 304–312.
[26] Z. Chen, P. Sun, B. Fan, Z. Zhang, X. Fang, J. Phys. Chem. C 118 (2014) 7801–7807.
[27] L. Bi, X. Gao, L. Zhang, D. Wang, X. Zou, T. Xie, ChemSusChem 11 (2017) 276–284.
[28] Y.T. Lu, D.M. Chu, M.S. Zhu, Y.K. Du, P. Yang, Phys. Chem. Chem. Phys. 17 (2015) 17355–17361.
[29] J.X. Low, C.J. Jiang, B. Cheng, S. Wageh, A.A. Al-Ghamdi, J.G. Yu, Small Methods 1 (2017) 1700080–1700101.
[30] X. Shi, M. Fujitsuka, S. Kim, T. Majima, Small 14 (2018) 1703277–1703286.
[31] X. Wang, K. Maeda, A. Thomas, K. Takanabe, G. Xin, J.M. Carlsson, K. Domen, M. Antonietti, Nat. Mater. 8 (2009) 76–80.
[32] G. Zhang, Z.-A. Lan, L. Lin, S. Lin, X. Wang, Chem. Sci. 7 (2016) 3062–3066.
[33] Q. Xiang, J. Yu, M. Jaroniec, J. Am. Chem. Soc. 134 (2012) 6575–6578.
[34] X. Zong, H. Yan, G. Wu, G. Ma, F. Wen, L. Wang, C. Li, J. Am. Chem. Soc. 130 (2008) 7176–7177.
[35] Y. Chen, Z. Qin, Catal. Sci. Technol. 6 (2016) 8212–8221.
[36] Y. Hou, Y. Zhu, Y. Xu, X. Wang, Appl. Catal. B-Environ. 156 (2014) 122–127.
[37] H. Ramakrishna Matte, A. Gomathi, A.K. Manna, D.J. Late, R. Datta, S.K. Pati, C. Rao, Angew. Chem. Int. Ed. 49 (2010) 4059–4062.
[38] M. Pumera, Z. Sofer, A. Ambrosi, J. Mater. Chem. A 2 (2014) 8981–8987.
[39] Y. Hou, A.B. Laursen, J. Zhang, G. Zhang, Y. Zhu, X. Wang, S. Dahl, I. Chorkendorff, Angew. Chem. Int. Ed. 52 (2013) 3621–3625.
[40] T.F. Jaramillo, K.P. Jørgensen, J. Bonde, J.H. Nielsen, S. Horch, I. Chorkendorff, Science 317 (2007) 100–102.
[41] A. Ambrosi, Z. Sofer, M. Pumera, Chem. Commun. 51 (2015) 8450–8453.
[42] J. Kibsgaard, Z. Chen, B.N. Reinecke, T.F. Jaramillo, Nat. Mater. 11 (2012) 963–969.
[43] H. Zhao, Y. Dong, P. Jiang, H. Miao, G. Wang, J. Zhang, J. Mater. Chem. A 3 (2015) 7375–7381.
[44] M.A. Lukowski, A.S. Daniel, F. Meng, A. Forticaux, L. Li, S. Jin, J. Am. Chem. Soc. 135 (2013) 10274–10277.
[45] C. Tsai, K. Chan, F. Abild-Pedersen, J.K. Nørskov, Phys. Chem. Chem. Phys. 16 (2014) 13156–13164.
[46] Y. Qu, H. Pan, C.T. Kwok, Z. Wang, Phys. Chem. Chem. Phys. 17 (2015) 24820–24825.
[47] H. Pan, Sci. Rep. 4 (2014) 5348.
[48] Y. Qu, H. Pan, C.T. Kwok, Z. Wang, Nanoscale Res. Lett. 10 (2015) 480.
[49] H. Pan, J. Phys. Chem. C 118 (2014) 13248–13253.
[50] J. Yuan, J. Wu, W.J. Hardy, P. Loya, M. Lou, Y. Yang, S. Najmaei, M. Jiang, F. Qin, K. Keyshar, Adv. Mater. 27 (2015) 5605–5609.
[51] Y. Qu, M. Shao, Y. Shao, M. Yang, J. Xu, C.T. Kwok, X. Shi, Z. Lu, H. Pan, J. Mater. Chem. A 5 (2017) 15080–15086.
[52] H. Liang, H. Shi, D. Zhang, F. Ming, R. Wang, J. Zhuo, Z. Wang, Chem. Mater. 28 (2016) 5587–5591.
[53] J. Liu, Q. Jia, J. Long, X. Wang, Z. Gao, Q. Gu, Appl. Catal. B-Environ. 222 (2018) 35–43.
[54] S.-S. Yi, J.-M. Yan, B.-R. Wulan, S.-J. Li, K.-H. Liu, Q. Jiang, Appl. Catal. B-Environ. 200 (2017) 477–483.
[55] L. Ming, H. Yue, L. Xu, F. Chen, J. Mater. Chem. A 2 (2014) 19145–19149.
[56] X. Bai, L. Wang, R. Zong, Y. Zhu, J. Phys. Chem. C 117 (2013) 9952–9961.
[57] W. Xiong, Z.Y. Wang, J.Q. Zhang, C.Q. Shang, M.Y. Yang, L.Q. He, Z.G. Lu, Energy Storage Mater. 7 (2017) 229–235.
[58] Y. Hou, Z. Wen, S. Cui, X. Guo, J. Chen, Adv. Mater. 25 (2013) 6291–6297.
[59] X. Zhong, L. Zhang, J. Tang, J. Chai, J. Xu, L. Cao, M. Yang, M. Yang, W. Kong, S. Wang, J. Mater. Chem. A 5 (2017) 17954–17962.
[60] J. Li, B. Shen, Z. Hong, B. Lin, B. Gao, Y. Chen, Chem. Commun. 48 (2012) 12017–12019.
[61] Y. Qu, M. Yang, J. Chai, Z. Tang, M. Shao, C.T. Kwok, M. Yang, Z. Wang, D. Chua, S. Wang, ACS Appl. Mater. Inter. 9 (2017) 5959–5967.
[62] M.S. Zhu, S. Kim, L. Mao, M. Fujitsuka, J.Y. Zhang, X.C. Wang, T. Majima, J. Am. Chem. Soc. 139 (2017) 13234–13242.
[63] Z.Y. Zhang, K.C. Liu, Z.Q. Feng, Y.N. Bao, B. Dong, Sci. Rep. 6 (2016) 19221.
[64] J. Ran, G. Gao, F.-T. Li, T.-Y. Ma, A. Du, S.-Z. Qiao, Nat. Commun. 8 (2017) 13907–13917.
[65] S. Chu, Y. Wang, Y. Guo, J. Feng, C. Wang, W. Luo, X. Fan, Z. Zou, ACS Catal. 3 (2013) 912–919.
[66] M. Shao, Y. Shao, J. Chai, Y. Qu, M. Yang, Z. Wang, M. Yang, W.F. Ip, C.T. Kwok, X. Shi, J. Mater. Chem. A 5 (2017) 16748–16756.
[67] J.K. Nørskov, T. Bligaard, J. Rossmeisl, C.H. Christensen, Nat. Chem. 1 (2009) 37–46.
[68] B. Hinnemann, P.G. Moses, J. Bonde, K.P. Jørgensen, J.H. Nielsen, S. Horch, I. Chorkendorff, J.K. Nørskov, J. Am. Chem. Soc. 127 (2005) 5308–5309.
[69] M. Jakob, H. Levanon, P.V. Kamat, Nano Lett. 3 (2003) 353–358.
[70] H. Li, C. Tsai, A.L. Koh, L. Cai, A.W. Contryman, A.H. Fragapane, J. Zhao, H.S. Han, H.C. Manoharan, F. Abild-Pedersen, Nat. Mater. 15 (2016) 48–53.
[71] J. Bonde, P.G. Moses, T.F. Jaramillo, J.K. Nørskov, I. Chorkendorff, Faraday Discuss. 140 (2009) 219–231.